Luo *et al.*
Protection and Control of Modern Power Systems (2023) 8:35
https://doi.org/10.1186/s41601-023-00302-0

Protection and Control of
Modern Power Systems

ORIGINAL RESEARCH **Open Access**

Transient synchronous stability analysis and enhancement control strategy of a PLL-based VSC system during asymmetric grid faults

Yi Luo[1], Jun Yao[1*], Zhaoyang Chen[1], Sen Huang[1], Shiyue Chen[2], Qi Zhang[1] and Zhentao Qin[1]

Abstract
The stability of a voltage source converters (VSC) system based on phase-locked loop (PLL) is very important issue during asymmetric grid faults. This paper establishes a transient synchronous stability model of a dual-sequence PLL-based VSC system during low voltage ride-through by referring to the equivalent rotor swing equation of synchronous generators. Based on the model, the synchronization characteristics of the VSC system under asymmetric grid faults are described, and the interaction mechanisms, as well as the transient instability phenomena of positive and negative sequence PLL during asymmetric faults are explained. Using the equal area criterion, the influences of sequence control switching action, detection delay, and interaction between the positive and negative sequence PLL on the transient synchronous stability of the VSC system are analyzed, respectively. In addition, a transient stability assessment criterion based on the critical fault clearance angle and time and an enhancement control strategy based on the improved positive and negative sequence PLL are proposed. Finally, the analytical results are validated through simulation and experiments.

Keywords Voltage source converters (VSC), Asymmetric grid faults, Dual-sequence PLL, Transient synchronous stability, Assessment criterion, Enhancement control strategy

1 Introduction

With the depletion of traditional fossil energy, renewable power generation (RPG) technology represented by wind power and photovoltaics has developed rapidly [1]. However, owing to the distribution of renewable energy resources, a large number of renewable energy plants are located in remote areas and are connected to the grids via long transmission lines, which are prone to short-circuit faults, especially asymmetric grid faults [2–5]. In addition, the latest grid codes in many countries have raised the requirements of reactive power support for RPG systems during the period of asymmetric grid faults [6, 7]. Consequently, studies on the transient stability of RPG during asymmetric grid faults are crucial.

Recently, loss of synchronization (LOS) events between RPG systems and grids have been reported many times [8], and have attracted widespread concern. For the transient stability of an RPG system under grid faults, existing researches mainly focused on two aspects. One is the existence of an equilibrium point, and the other is the ability of the system to reach a new equilibrium point after faults [9]. Voltage source converters (VSC) are widely used in the grid-connected interface of an RPG

*Correspondence:
Jun Yao
topyj@163.com
[1] State Key Laboratory of Power Transmission Equipment and System Security and New Technology, School of Electrical Engineering, Chongqing University, Chongqing 400044, China
[2] State Grid Changzhou Power Supply Company, Changzhou 2131261, China

system, such as wind power and photovoltaics, and reference [10] investigates the transient stability of the VSC system during symmetric grid faults, and indicates that LOS is inevitable in the absence of an equilibrium point when a grid fault occurs. In addition, references [11, 12] find that the phase of the terminal voltage is a key factor that influences the existence of an equilibrium point for an RPG system, and there is the coupling phenomenon between the terminal voltage and frequency of the system. However, even if the equilibrium point exists [13, 14], an improper initial state or poor dynamic characteristics of the system can lead to LOS. References [15–18] point out that intense interaction behaviors between PLL and the grid can lead to transient instability for the system. By using a Lyapunov function [19] and the equal area criterion (EAC), references [14, 20] establish the large signal models of a VSC system, which is similar to the rotor swing equation of an SG, and explain the physical mechanism of transient instability of the system at different fault stages. However, these studies only explore the transient stability of the VSC system during a symmetric fault, while most of short circuit faults in power systems are asymmetric [21].

Compared with the transient operational characteristics under symmetric grid faults, those of an RPG system under asymmetric grid faults are more complex. References [22] indicates that during asymmetric grid faults, RPG system not only has positive, negative and zero sequence components simultaneously, but also has a coupling relationship between the positive and negative sequence components. Moreover, references [23] further points out that both the positive and negative sequence components of the system have the ability to keep synchronization with the grid during asymmetric grid faults, which need to be controlled individually and precisely. Therefore, in [24–26], the decoupled double synchronous reference frame PLL (DDSRF-PLL) models are established to accurately control the transient components of the system, and study the influence of the positive and negative sequence reactive currents injection on the transient stability of the system during asymmetric grid faults. However, in the above studies, the negative angular frequency is considered to be the inverse of the positive angular frequency. References [26] points out that the output angle of the negative sequence PLL is significantly different from that of positive sequence PLL during asymmetric grid faults, and so needs to be studied separately. In addition, it is a prerequisite for analyzing the transient stability of a VSC system to accurately depict the operating characteristics of the system under grid faults [27, 28]. However, the above studies rarely consider the influence of fault detection delay, nonlinear control behaviors [29] and other factors on the transient stability of a VSC system under unbalanced fault conditions. Therefore, it is difficult to accurately depict the transient synchronous stability process of the VSC system during asymmetric grid faults.

To fill the gaps, this paper aims to reveal the influence of sequence control switching action, fault detection delay and interaction between the positive and negative sequence components on the transient synchronous stability of the PLL-based grid connected VSC system during asymmetric grid faults. Based on previous analyses, a corresponding transient stability criterion and enhancement control strategy are proposed. The main contributions of this paper are as follows:

1. A novel large-signal model and analysis method for the dual-sequence transient synchronization stability of the VSC system are presented, one which considers the coupled characteristics between the positive and negative sequence components and the nonlinear control characteristics of PLL.
2. Considering the influence mechanism of sequence control switching action, detection delay and interaction between the positive and negative sequence PLL on the transient behaviors and instability phenomenon of a VSC system, a novel transient synchronous stability evaluation criterion for the VSC system during asymmetric grid faults is proposed.
3. By increasing the critical fault clearance time and reducing detection delay time, an enhancement control strategy for a VSC system under asymmetric grid faults is proposed, one which is based on the improved positive and negative sequence PLL.

The rest of the paper is structured as follows: Sect. 2 depicts the transient characteristics of a VSC system during asymmetric faults, while Sect. 3 analyzes the transient synchronous mechanism, instability criterion and enhancement control strategy of the system during asymmetric grid faults. In Sect. 4, the simulation and experimental results are presented, and Sect. 5 concludes the paper.

2 Transient characteristics of the VSC systems during asymmetric faults

Figure 1 shows the control block diagram of the PLL-based VSC system under asymmetric grid faults, in which the transformer T_1 adopts the Y/Δ connection type. During the pre-fault period, the external power control loop and internal current control loop structures are used to realize maximum power point tracking (MPPT) control (Flag = 1). When the grid voltage ($\boldsymbol{U}_g$) dip is detected, the VSC system only adopts the

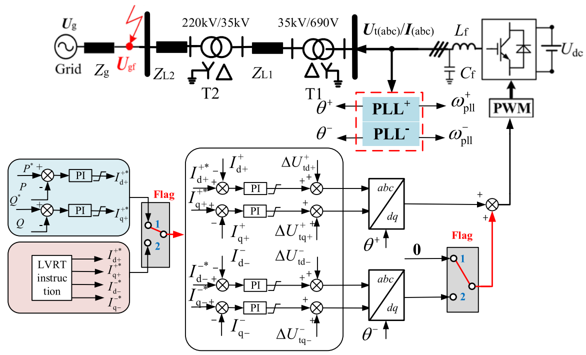

Fig. 1 The control block diagram of a VSC system under asymmetric grid faults

single current loop control (Flag = 2), to realize the rapid injection of positive and negative sequence reactive currents during LVRT.

Since the analysis methods adopted in this paper are applicable to all types of asymmetric grid faults, the transient stability of the VSC system during asymmetric faults is analyzed in detail by taking the single-line-to-ground (SLG) fault as an example. When an SLG fault occurs, the VSC system has all of positive, negative and zero sequence components [21]. However, since both transformers T_1 and T_2 adopt the Y/Δ connection type, there is no zero-sequence path in the system. Therefore, this paper only considers the influence of the positive and negative sequence components on the terminal voltage ($\boldsymbol{U}_t$). This can be expressed as:

$$\boldsymbol{U}_{\mathrm{t}} = \boldsymbol{U}_{\mathrm{t}}^{+} + \boldsymbol{U}_{\mathrm{t}}^{-} \tag{1}$$

Since the output angle of the negative sequence PLL is significantly different from that of the positive sequence PLL during asymmetric grid faults [23], positive and negative sequence PLL should be established to accurately track the positive and negative sequence grid voltages, respectively. Here, a $dq_{\pm}$ reference frame is established, as shown in Fig. 2.

Considering the coupled characteristics between the positive and negative sequence components, the composite sequence network diagram [23] of the VSC system when an SLG fault occurs is shown in Fig. 3. As shown, considering that the RPG source with the VSC as the interface is not directly connected to the grid, but through large DC-link capacitance, this makes the sources have excellent anti-disturbance ability for grid voltage. Meanwhile, as the grid faults occur within a short time from tens of milliseconds to hundreds of milliseconds, control schemes [30] can be adopted by the converter between the generating source and the DC-link capacitance to maintain the DC-link voltage as stable during the faults. Consequently, the DC-link voltage can be assumed to be stable during grid faults [9, 10], and the characteristics of the generating sources will not affect the transient stability of the VSC system. Therefore, the positive and negative sequence currents provided by the VSC system are regarded as the controlled current sources $\boldsymbol{I}^{+}$ and $\boldsymbol{I}^{-}$ with frequencies of $\omega_{\mathrm{pll}}^{+}$ and $\omega_{\mathrm{pll}}^{-}$, respectively. Z_{t}^{+} and Z_{t}^{-} are regarded as the positive and negative sequence equivalent impedances of the filter circuit, respectively. In addition, the positive sequence current source provides over-excited reactive power, while the negative sequence current source provides under-excited reactive power [23]. The currents injected by the system can be expressed as:

$$\begin{cases} \boldsymbol{I} = \boldsymbol{I}^{+} + \boldsymbol{I}^{-} \\ \boldsymbol{I}^{+} = I^{+}\angle(\theta^{+} + \theta_{0}^{+}) \\ \boldsymbol{I}^{-} = I^{-}\angle(\theta^{-} + \theta_{0}^{-}) \end{cases} \tag{2}$$

where θ_0^{+} and θ_0^{-} are the angles of $\boldsymbol{I}^{+}$ in the dq_{+} reference frame and $\boldsymbol{I}^{-}$ in the dq_{-} reference frame, respectively. θ^{+} is the angle between the α and d_{+} axes, while θ^{-} is the angle between the α and d_{-} axes. In addition, the superscript represents the positive and negative sequence components, while the subscript represents the $dq_{\pm}$ reference frame.

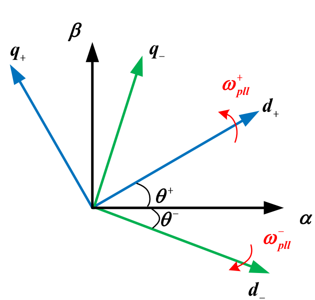

Fig. 2 Spatial position diagram of PLL $dq_{\pm}$ reference frames

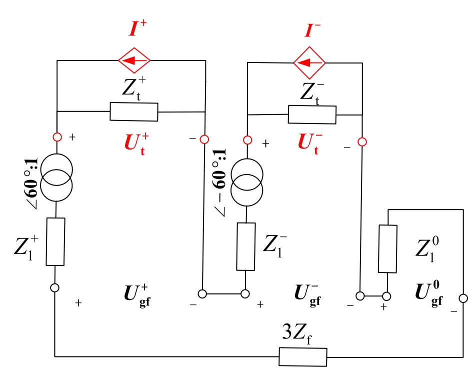

Fig. 3 Sequence domain circuit under SLG fault

From Fig. 3, $\boldsymbol{U}_{\mathrm{t}}$ can be shown as:

$$\begin{cases} \boldsymbol{U}_{\mathbf{t}}^{+} = K_1\boldsymbol{U}_{\mathrm{gf}}^{+}\mathrm{e}^{-\mathrm{j}\frac{\pi}{3}} - K_2\boldsymbol{U}_{\mathrm{gf}}^{-}\mathrm{e}^{-\mathrm{j}\frac{\pi}{3}} - K_3\boldsymbol{U}_{\mathrm{gf}}^{0}\mathrm{e}^{-\mathrm{j}\frac{\pi}{3}} + \boldsymbol{I}^{+}Z_4 - \boldsymbol{I}^{-}Z_5\mathrm{e}^{-\mathrm{j}\frac{2\pi}{3}} \\ \boldsymbol{U}_{\mathbf{t}}^{-} = -K_6\boldsymbol{U}_{\mathrm{gf}}^{+}\mathrm{e}^{\mathrm{j}\frac{\pi}{3}} + K_7\boldsymbol{U}_{\mathrm{gf}}^{-}\mathrm{e}^{\mathrm{j}\frac{\pi}{3}} - K_8\boldsymbol{U}_{\mathrm{gf}}^{0}\mathrm{e}^{\mathrm{j}\frac{\pi}{3}} + \boldsymbol{I}^{+}Z_9 - \boldsymbol{I}^{-}Z_{10}\mathrm{e}^{\mathrm{j}\frac{2\pi}{3}} \end{cases} \tag{3}$$

where $K_{\mathrm{i}}=|K_{\mathrm{i}}|\angle\varphi_{\mathrm{i}}$, i = 1, 2, 3, 6, 7, and 8, and $Z_{\mathrm{i}}=|Z_{\mathrm{i}}|\angle\phi_{\mathrm{i}}$, i = 4, 5, 9 and 10, as summarized in the Appendix.

When the terminal voltage is excited by the positive or negative sequence current of the system, it will have the same frequency as the excitation current and its conjugate quantity [22]. In addition, since $\boldsymbol{U}_{\mathrm{gf}}{}^{0}$ cannot stimulate the corresponding fault current at the terminal of the system, its effect can be ignored. Therefore, transforming (3) into the $dq_{\pm}$ reference frame yields:

$$\begin{cases} u_{\mathrm{td}+}^{+} + \mathrm{j}u_{\mathrm{tq}+}^{+} = |K_1|U_{\mathrm{gf}}^{+}\angle(\varphi_1-\delta^{+}) - K_2U_{\mathrm{gf}}^{-}\angle(\varphi_2-\delta^{+}+\delta^{-}) + I^{+}|Z_4|\angle(\varphi_4+\theta_0^{+}) \\ \qquad -I^{-}|Z_5|\angle(\varphi_5+\theta_0^{-}-\delta^{+}+\delta^{-}) - \mathrm{conj}(I^{-}|Z_5|\angle(\varphi_5+\theta^{-})) \\ u_{\mathrm{td}-}^{-} + \mathrm{j}u_{\mathrm{tq}-}^{-} = -|K_6|U_{\mathrm{gf}}^{+}\angle(\varphi_6+\delta^{+}-\delta^{-}) + K_7U_{\mathrm{gf}}^{-}\angle(\varphi_7-\delta^{-}) + |Z_9|I^{-}\angle(\varphi_9+\theta_0^{-}) \\ \qquad -|Z_{10}|I^{+}\angle(\varphi_{10}+\theta_0^{+}+\delta^{+}-\delta^{-}) - \mathrm{conj}(|Z_{10}|I^{+}\angle(\varphi_{10}+\theta^{+})) \end{cases} \tag{4}$$

where δ^{+} is the angle difference between the positive sequence terminal voltage ($\boldsymbol{U}_{\mathrm{t}}^{+}$) and grid voltage ($\boldsymbol{U}_{\mathrm{gf}}^{+}$), and δ^{-} is the angle difference between $\boldsymbol{U}_{\mathrm{t}}^{-}$ and $\boldsymbol{U}_{\mathrm{gf}}^{-}$, conj($I^{-}$ $|Z_5|$ $\angle(\phi_5$-$\theta^{-})$) is the coupled voltage component generated by the negative sequence current, while conj($I^{+}|Z_{10}|\angle(\phi_{10}$-$\theta^{+})$) is the coupled voltage component generated by the positive sequence current.

To eliminate the double frequency components in the $dq_{\pm}$ reference frame, the moving average filter (MAF) is widely used to extract the positive and negative sequence components [31]. Therefore, a dual-sequence PLL model based on MAF is established in this paper, as shown in Fig. 4.

According to the PLL control structure, the dynamic model of the positive and negative sequence PLL can be obtained as:

$$\begin{cases} \omega_{\mathrm{pll}}^{+} = k_{\mathrm{p}}U_{\mathrm{tq}+}^{+} + k_{\mathrm{i}}\int U_{\mathrm{tq}+}^{+}dt + \omega_{\mathrm{g}} \\ \frac{d\omega_{\mathrm{pll}}^{+}}{dt} = k_{\mathrm{p}}\frac{dU_{\mathrm{tq}+}^{+}}{dt} + k_{\mathrm{i}}U_{\mathrm{tq}+}^{+} \end{cases} \tag{5}$$

$$\begin{cases} \omega_{\mathrm{pll}}^{-} = k_{\mathrm{p}}U_{\mathrm{tq}-}^{-} + k_{\mathrm{i}}\int U_{\mathrm{tq}-}^{-}dt - \omega_{\mathrm{g}} \\ \frac{d\omega_{\mathrm{pll}}^{-}}{dt} = k_{\mathrm{p}}\frac{dU_{\mathrm{tq}-}^{-}}{dt} + k_{\mathrm{i}}U_{\mathrm{tq}-}^{-} \end{cases} \tag{6}$$

The change rate of $u_{\mathrm{tq}+}^{+}$ and $u_{\mathrm{tq}-}^{-}$ can be expressed as:

$$\begin{cases} \frac{du_{\mathrm{tq}+}^{+}}{dt} = -U_{\mathrm{gf}}^{+}|K_1|\cos(\delta^{+}-\varphi_1)\frac{d\delta^{+}}{dt} + L_{\mathrm{eq4}}I_{\mathrm{d}+}^{+}\frac{d\omega_{\mathrm{pll}}^{+}}{dt} - L_{\mathrm{eq5}}I_{\mathrm{d}+}^{-}\frac{d\omega_{\mathrm{pll}}^{-}}{dt} \\ \frac{du_{\mathrm{tq}-}^{-}}{dt} = -U_{\mathrm{gf}}^{-}|K_7|\cos(\delta^{-}-\varphi_7)\frac{d\delta^{-}}{dt} + L_{\mathrm{eq9}}I_{\mathrm{d}-}^{-}\frac{d\omega_{\mathrm{pll}}^{-}}{dt} - L_{\mathrm{eq10}}I_{\mathrm{d}-}^{+}\frac{d\omega_{\mathrm{pll}}^{+}}{dt} \end{cases} \tag{7}$$

where $L_{\mathrm{eq4}}=(\mathrm{Z}_4\sin\phi_4)/(2\pi\omega_{\mathrm{pll}}^{+})$, $L_{\mathrm{eq5}}=(\mathrm{Z}_5\sin(\phi_5)/(2\pi\omega_{\mathrm{pll}}^{-})$, $L_{\mathrm{eq9}}=(\mathrm{Z}_9\sin\phi_9)/(2\pi\omega_{\mathrm{pll}}^{-})$, and $L_{\mathrm{eq10}}=(\mathrm{Z}_{10}\sin\phi_{10})/(2\pi\omega_{\mathrm{pll}}^{+})$.

Substituting (5) and (6) into (7), yields:

$$\begin{cases} \frac{d\omega_{\mathrm{pll}}^{+}}{dt} = k_{\mathrm{p}}(-U_{\mathrm{gf}}^{+}|K_1|\cos(\delta^{+}-\varphi_1)\frac{d\delta^{+}}{dt} + L_{\mathrm{eq4}}I_{\mathrm{d}+}^{+}\frac{d\omega_{\mathrm{pll}}^{+}}{dt} - L_{\mathrm{eq5}}I_{\mathrm{d}+}^{-}\frac{d\omega_{\mathrm{pll}}^{-}}{dt} \\ \qquad +k_{\mathrm{i}}(-|K_1|U_{\mathrm{gf}}^{+}\sin(\delta^{+}-\varphi_1) + R_{\mathrm{eq4}}I_{\mathrm{q}+}^{+} + \omega_{\mathrm{pll}}^{+}L_{\mathrm{eq4}}I_{\mathrm{d}+}^{+} - R_{\mathrm{eq5}}I_{\mathrm{q}+}^{-} - \omega_{\mathrm{pll}}^{-}L_{\mathrm{eq5}}I_{\mathrm{d}+}^{-}) \\ \frac{d\omega_{\mathrm{pll}}^{-}}{dt} = k_{\mathrm{p}}(-U_{\mathrm{gf}}^{-}|K_7|\cos(\delta^{-}-\varphi_7)\frac{d\delta^{-}}{dt} + L_{\mathrm{eq9}}I_{\mathrm{d}-}^{-}\frac{d\omega_{\mathrm{pll}}^{-}}{dt}L_{\mathrm{eq10}}I_{\mathrm{d}-}^{+}\frac{d\omega_{\mathrm{pll}}^{+}}{dt}) \\ \qquad +k_{\mathrm{i}}(-|K_7|U_{\mathrm{gf}}^{-}\sin(\delta^{-}-\varphi_7) + R_{\mathrm{eq9}}I_{\mathrm{q}-}^{-} + \omega_{\mathrm{pll}}^{-}L_{\mathrm{eq9}}I_{\mathrm{d}-}^{-} - R_{\mathrm{eq10}}I_{\mathrm{q}-}^{+} - \omega_{\mathrm{pll}}^{+}L_{\mathrm{eq10}}I_{\mathrm{d}-}^{+}) \end{cases} \tag{8}$$

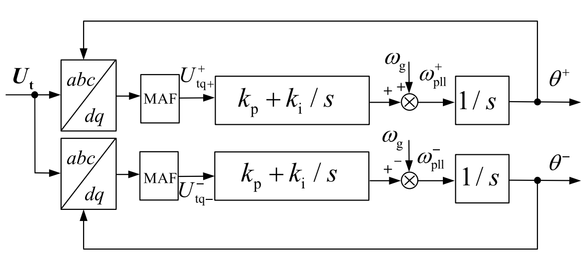

Fig. 4 PLL control structure based on positive and negative sequence separation

From (5) and (6), δ^{+} and δ^{-} can be expressed as:

$$\begin{cases} \frac{d\delta^{+}}{dt} = \omega_{\mathrm{b}}(\omega_{\mathrm{pll}}^{+} - \omega_{\mathrm{g}}) \\ \frac{d\delta^{-}}{dt} = \omega_{\mathrm{b}}(\omega_{\mathrm{pll}}^{-} + \omega_{\mathrm{g}}) \end{cases} \tag{9}$$

By referring to the SG, the positive and negative sequence transient synchronous characteristics of the VSC system can be obtained as (10), where $R_{\mathrm{eq4}}=Z_4\cos\phi_4$, $R_{\mathrm{eq5}}=Z_5\cos\phi_5$, $R_{\mathrm{eq9}}=Z_9\cos\phi_9$, $R_{\mathrm{eq10}}=Z_{10}\cos\phi_{10}$.

In (10), $J_{\mathrm{v}+}^{+}$ and $D_{\mathrm{v}+}^{+}$ are the positive sequence virtual inertia and damping coefficients, respectively, whereas, $J_{\mathrm{v}+}^{-}$ and $D_{\mathrm{v}+}^{-}$ are the negative sequence coupled virtual inertia and damping coefficient, respectively. These reflect the influence of the negative sequence components on the transient stability of the positive sequence PLL. In addition, $J_{\mathrm{v}-}^{-}$ and $D_{\mathrm{v}-}^{-}$ are the negative sequence virtual inertia and damping coefficients, respectively, while $J_{\mathrm{v}-}^{+}$ and $D_{\mathrm{v}+}^{-}$ are the positive sequence coupled virtual inertia and damping coefficient, respectively. These reflect the influence of the positive sequence components on the transient stability of negative sequence PLL. Furthermore, $T_{\mathrm{v}+}^{*}$ and $T_{\mathrm{v}+}^{+}$ are the positive sequence virtual prime mover torque and electromagnetic torque, respectively. Similarly, $T_{\mathrm{v}-}^{*}$ and $T_{\mathrm{v}-}^{-}$ are the negative sequence virtual prime mover and electromagnetic torque, respectively.

In addition, it can be seen in (10) that $T_{\mathrm{v}+}^{*}$ consists of the positive sequence prime mover torque $(R_{\mathrm{eq}4}I_{\mathrm{q}+}^{+} + \omega_{\mathrm{g}}L_{\mathrm{eq}4}I_{\mathrm{d}+}^{+})$ and the negative sequence coupled prime mover torque $(R_{\mathrm{eq}5}I_{\mathrm{q}+}^{-} + \omega_{g}L_{\mathrm{eq}5}I_{\mathrm{d}+}^{-})$. This reflects the interaction between the positive sequence output power and grid. Similarly, $T_{\mathrm{v}-}^{*}$ consists of the negative sequence prime mover torque $(R_{\mathrm{eq}9}I_{\mathrm{q}-}^{-} - \omega_{\mathrm{g}}L_{\mathrm{eq}9}I_{\mathrm{d}-}^{-})$ and the positive sequence coupled prime mover torque $(R_{\mathrm{eq}10}I_{\mathrm{q}-}^{+} + \omega_{\mathrm{g}}L_{\mathrm{eq}10}I_{\mathrm{d}-}^{+})$, and this reflects the interaction between the negative sequence output power and grid. $T_{\mathrm{v}+}^{+}$ and $T_{\mathrm{v}-}^{-}$ reflect the clamping effect of the positive and negative sequence grid voltage on the transient stability of the system, respectively.

From (10), the positive and negative sequence nonlinear dynamic control model can be obtained, as shown in Fig. 5. Although the positive and negative sequence PLL models are established separately in this paper, under the interaction between the PLL and grid, the dynamic behavior of positive and negative sequence PLL will influence each other during the faults. As shown in (10) and Fig. 5, under the actions of the coupled prime mover $(R_{\mathrm{eq}10}I_{\mathrm{q}-}^{+} + \omega_{\mathrm{g}}L_{\mathrm{eq}10}I_{\mathrm{d}-}^{+})$ or $(R_{\mathrm{eq}5}I_{\mathrm{q}+}^{-} + \omega_{g}L_{\mathrm{eq}5}I_{\mathrm{d}+}^{-})$, when the working state of the positive or negative sequence PLL changes, the unbalanced virtual torque $\Delta T_{\mathrm{v}+}$ and $\Delta T_{\mathrm{v}-}$ will occur simultaneously. In these conditions, $\Delta T_{\mathrm{v}+}$ or $\Delta T_{\mathrm{v}-}$ will lead both $\omega_{\mathrm{pll}}^{+}$ and $\omega_{\mathrm{pll}}^{-}$ to change. δ^{-} and δ^{+} also will also tend to change. Then, through the negative feedback branches, δ^{-} and δ^{+} will adjust $T_{\mathrm{v}+}^{+}$ and $T_{\mathrm{v}-}^{-}$ to eliminate $\Delta T_{\mathrm{v}\pm}$. Finally, if $\Delta T_{\mathrm{v}+}$ and $\Delta T_{\mathrm{v}-}$ are both eliminated, $\omega_{\mathrm{pll}}^{+}$ and $\omega_{\mathrm{pll}}^{-}$ will be restored to the corresponding ω_{g} and $-\omega_{\mathrm{g}}$ under the actions of the damping coefficients ($D_{\mathrm{v}+}^{+}$, $D_{\mathrm{v}+}^{-}$, $D_{\mathrm{v}-}^{+}$, and $D_{\mathrm{v}-}^{-}$). In addition, due to the existence of coupled virtual damping coefficients ($D_{\mathrm{v}+}^{-}$, $D_{\mathrm{v}-}^{+}$), the positive or negative sequence PLL will provide damping effect on the transient synchronization of the other PLL.

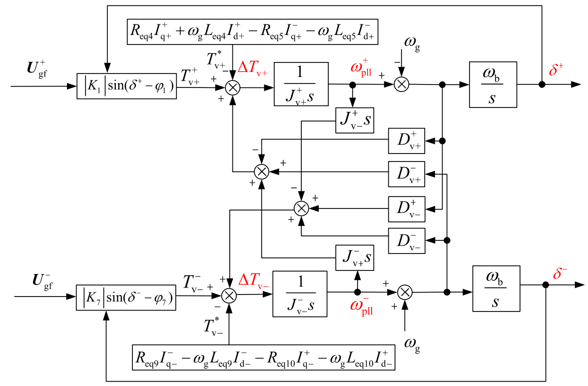

Fig. 5 Equivalent dynamic control model of the VSC system

$$
\left\{
\begin{aligned}
&\underbrace{\left(\frac{1-k_{\mathrm{p}}L_{\mathrm{eq}4}I_{\mathrm{d}+}^{+}}{k_{\mathrm{i}}}\right)}_{J_{\mathrm{v}+}^{+}}\frac{d\omega_{\mathrm{pll}}^{+}}{dt}+\underbrace{\frac{k_{\mathrm{p}}L_{\mathrm{eq}5}I_{\mathrm{d}+}^{-}}{k_{\mathrm{i}}}}_{J_{\mathrm{v}+}^{-}}\frac{d\omega_{\mathrm{pll}}^{-}}{dt}=\underbrace{R_{\mathrm{eq}4}I_{\mathrm{q}+}^{+}+\omega_{\mathrm{g}}L_{\mathrm{eq}4}I_{\mathrm{d}+}^{+}-R_{\mathrm{eq}5}I_{\mathrm{q}+}^{-}-\omega_{\mathrm{g}}L_{\mathrm{eq}5}I_{\mathrm{d}+}^{-}}_{T_{\mathrm{v}+}^{*}}-\underbrace{U_{\mathrm{gf}}^{+}|K_1|\sin(\delta^{+}-\varphi_1)}_{T_{\mathrm{v}+}^{+}}\\
&+\underbrace{\left(\frac{k_{\mathrm{p}}}{k_{\mathrm{i}}}L_{\mathrm{eq}5}I_{\mathrm{d}+}^{-}\right)}_{D_{\mathrm{v}+}^{-}}(\omega_{\mathrm{pll}}^{-}+\omega_{\mathrm{g}})-\underbrace{\left(\frac{k_{\mathrm{p}}}{k_{\mathrm{i}}}(\omega_{\mathrm{b}}U_{\mathrm{gf}}^{+}|K_1|\cos(\varphi_1-\delta^{+})-L_{\mathrm{eq}4}I_{\mathrm{d}+}^{+})\right)}_{D_{\mathrm{v}+}^{+}}(\omega_{\mathrm{pll}}^{+}-\omega_{\mathrm{g}})\\
&\underbrace{\left(\frac{1-k_{\mathrm{p}}L_{\mathrm{eq}9}I_{\mathrm{d}-}^{-}}{k_{\mathrm{i}}}\right)}_{J_{\mathrm{v}-}^{-}}\frac{d\omega_{\mathrm{pll}}^{-}}{dt}+\underbrace{\frac{k_{\mathrm{p}}L_{\mathrm{eq}10}I_{\mathrm{d}-}^{+}}{k_{\mathrm{i}}}}_{J_{\mathrm{v}-}^{+}}\frac{d\omega_{\mathrm{pll}}^{+}}{dt}=\underbrace{R_{\mathrm{eq}9}I_{\mathrm{q}-}^{-}-\omega_{\mathrm{g}}L_{\mathrm{eq}9}I_{\mathrm{d}-}^{-}-R_{\mathrm{eq}10}I_{\mathrm{q}-}^{+}-\omega_{\mathrm{g}}L_{\mathrm{eq}10}I_{\mathrm{d}-}^{+}}_{T_{\mathrm{v}-}^{*}}-\underbrace{U_{\mathrm{gf}}^{-}|K_7|\sin(\delta^{-}-\varphi_7)}_{T_{\mathrm{v}-}^{-}}+\underbrace{\left(\frac{k_{\mathrm{p}}}{k_{\mathrm{i}}}L_{\mathrm{eq}10}I_{\mathrm{d}-}^{+}\right)}_{D_{\mathrm{v}-}^{+}}(\omega_{\mathrm{pll}}^{+}-\omega_{\mathrm{g}})\\
&-\underbrace{\left(\frac{k_{\mathrm{p}}}{k_{\mathrm{i}}}(\omega_{\mathrm{b}}U_{\mathrm{gf}}^{-}|K_7|\cos(\varphi_7-\delta^{-})-L_{\mathrm{eq}9}I_{\mathrm{d}-}^{-})\right)}_{D_{\mathrm{v}-}^{-}}(\omega_{\mathrm{pll}}^{-}+\omega_{\mathrm{g}})
\end{aligned}
\right. \tag{10}
$$

The dynamic behavior of the positive and negative sequence PLL during the fault means that they will influence each other. Thus, only if no LOS phenomenon occurs in either the positive or negative sequence PLL, the VSC system may maintain transient synchronous stability with the grid.

3 Analysis of the transient synchronous mechanism during asymmetric faults

According to the analysis presented in Sect. 2, the coupled relationship between the positive and negative sequence PLL, as well as the operating conditions of the system, can seriously affect the transient stability of the VSC system. Therefore, this section will further explore the influence mechanism of the interaction between the positive and negative sequence PLL, as well as the control switching action, on the existence of the equilibrium point and the transient synchronous process of the system. Considering that the mainstream grid fault detection methods have at least 5–20 ms of detection delay [32], therefore, this paper will also further explore the influence of fault detection delay on the transient characteristics of the VSC system during asymmetric grid faults.

3.1 Synchronous characteristics at fault detection stage

As assumed in Sect. 2, the VSC system works in MPPT and the unity power factor state during the pre-fault stage. When an SLG fault occurs, the current injected by the system during the fault detection stage is given as:

$$I_{\mathrm{d+}}^{+*}=\begin{cases}\dfrac{P_{\mathrm{n}}^{*}}{U_{\mathrm{tdf}}}, & \left(\dfrac{P_{\mathrm{n}}^{*}}{U_{\mathrm{tdf}}}<I_{\mathrm{dm}}\right)\\ I_{\mathrm{dm}}\ , & \left(\dfrac{P_{\mathrm{n}}^{*}}{U_{\mathrm{tdf}}}\geq I_{\mathrm{dm}}\right)\end{cases} \tag{11}$$

where I_{dm} is the current limiting value of the grid side converter (GSC).

Considering that although VSC is still working in Flag 1 mode at the fault detection stage, because of the weak anti-disturbance of power electronic devices, the fault current of the system will increase rapidly to the current threshold (I_{dm}) under severe grid faults. In this case, the outer power control loop will saturate and lose its function. As a result, $I_{\mathrm{d+}}^{+*}=I_{\mathrm{dm}}$ at the fault detection stage.

Since there is no requirement of the negative sequence active current in the latest grid codes [6, 7], the VSC system does not provide negative sequence active current in this paper. Therefore, when the LVRT strategy is triggered, the current references of the system will be set directly, as:

$$\begin{cases} I_{\mathrm{d+}}^{+}=I_{\mathrm{d+}}^{+*} & I_{\mathrm{q+}}^{+}=I_{\mathrm{q+}}^{+*}\\ I_{\mathrm{d-}}^{-}=I_{\mathrm{d-}}^{-*}=0 & I_{\mathrm{q-}}^{-}=I_{\mathrm{q-}}^{-*}\end{cases} \tag{12}$$

In addition, because of the detection delay of the system, the LVRT strategy of the system is not triggered immediately at the fault detection stage. Consequently, the system will still output current according to the instructions before the fault occurrence, which means that the system only provides active current at the fault detection stage.

In combination with (10)–(12), Eq. (13) can be obtained, which reflects the synchronous characteristics of the positive and negative sequence PLL at the fault detection stage.

$$\begin{cases}\underbrace{\left(\dfrac{1-k_{\mathrm{p}}L_{\mathrm{eq4}}I_{\mathrm{d+}}^{+}}{k_{\mathrm{i}}}\right)}_{J_{\mathrm{v+}}^{+}}\dfrac{d\omega_{\mathrm{pll}}^{+}}{dt}=\underbrace{\omega_{\mathrm{g}}L_{\mathrm{eq4}}I_{\mathrm{dm}}}_{T_{\mathrm{v+}}^{*}}-\underbrace{U_{\mathrm{gf}}^{+}|K_1|\sin(\delta^{+}-\varphi_1)}_{T_{\mathrm{v+}}^{+}}\\ -\underbrace{\left(\dfrac{k_{\mathrm{p}}}{k_{\mathrm{i}}}(\omega_{\mathrm{b}}U_{\mathrm{gf}}^{+}|K_1|\cos(\varphi_1-\delta^{+})-L_{\mathrm{eq4}}I_{\mathrm{dm}})\right)}_{D_{\mathrm{v+}}^{+}}(\omega_{\mathrm{pll}}^{+}-\omega_{\mathrm{g}})\\ \underbrace{\left(\dfrac{1}{k_{\mathrm{i}}}\right)}_{J_{\mathrm{v-}}^{-}}\dfrac{d\omega_{\mathrm{pll}}^{-}}{dt}+\underbrace{\dfrac{k_{\mathrm{p}}L_{\mathrm{eq10}}I_{\mathrm{dm}}}{k_{\mathrm{i}}}}_{J_{\mathrm{v-}}^{+}}\dfrac{d\omega_{\mathrm{pll}}^{+}}{dt}=\underbrace{-\omega_{\mathrm{g}}L_{\mathrm{eq10}}I_{\mathrm{dm}}}_{T_{\mathrm{v-}}^{*}}-\underbrace{U_{\mathrm{gf}}^{-}|K_7|\sin(\delta^{-}-\varphi_7)}_{T_{\mathrm{v-}}^{-}}\\ +\underbrace{\left(\dfrac{k_{\mathrm{p}}}{k_{\mathrm{i}}}L_{\mathrm{eq10}}I_{\mathrm{dm}}\right)}_{D_{\mathrm{v-}}^{+}}(\omega_{\mathrm{pll}}^{+}-\omega_{\mathrm{g}})-\underbrace{\left(\dfrac{k_{\mathrm{p}}}{k_{\mathrm{i}}}(\omega_{\mathrm{b}}U_{\mathrm{gf}}^{-}|K_7|\cos(\varphi_7-\delta^{-})\right)}_{D_{\mathrm{v-}}^{-}}(\omega_{\mathrm{pll}}^{-}+\omega_{\mathrm{g}})\end{cases} \tag{13}$$

3.2 Influence on the existence of positive and negative sequence equilibrium points

According to (10), the existence of the positive and negative sequence coupled components influences the virtual prime mover torque $T^*_{v\pm}$, while the interaction between $T^*_{v\pm}$ and $T^{\pm}_{v\pm}$ directly affects the balance of torque. Therefore, the interaction between the positive and negative sequence PLL will also significantly affect the existence of the positive and negative sequence equilibrium points, as well as the instability forms of the system. By analyzing the interaction relationships between $T^*_{v\pm}$ and $T^{\pm}_{v\pm}$, there are four cases where the positive and negative sequence equilibrium points of the VSC system do not exist. These are shown in Fig. 6a–d, respectively.

As shown in Fig. 6a, if the minimum value of T^+_{v+} is greater than T^*_{v+}, the unbalanced torque (ΔT_{v+}) will drive ω^+_{pll} to decrease. From Fig. 5, $|\omega^-_{pll}|$ will also decrease under the action of the positive sequence coupled components. Finally, the LOS phenomena for angular frequency decrease will occur in both the positive and negative sequence PLL. In addition, in this case, according to (10), the negative sequence coupled components prevent T^*_{v+} from moving downward. This is conducive to the transient stability of the system.

When the maximum value of T^+_{v+} is less than T^*_{v+}, as is shown in Fig. 6b, $(T^*_{v+}-T^+_{v+})>0$ will be always valid, and continue to drive ω^+_{pll} and $|\omega^-_{pll}|$ to increase, eventually leading to the LOS phenomena for angular frequency increase in the positive and negative sequence PLL. In this case, the negative sequence coupled components cause T^*_{v+} to move upward. This will deteriorate the transient stability of the system.

As shown in Fig. 6c, when the minimum value of T^-_{v-} is greater than T^*_{v-}, the negative sequence unbalanced torque (ΔT_{v-}) will make $|\omega^-_{pll}|$ and ω^+_{pll} increase continuously. Finally, the LOS phenomena for angular frequency increase will occur in the negative and positive sequence PLL. In this case, the positive sequence coupled components will cause T^*_{v-} to move down-ward, and deteriorate the transient stability of the system.

In Fig. 6d, if the maximum value of T^-_{v-} is less than T^*_{v-}, there will be no intersection between T^-_{v-} and T^*_{v-}. In this case, the surplus ΔT_{v-} will lead to the LOS phenomena for angular frequency decrease in the negative and positive sequence PLL. In addition, the positive sequence coupled components will prevent T^*_{v-} from moving upward. This is beneficial to the transient stability of the system.

In conclusion, the interaction between the positive and negative sequence components will significantly affect the balance of the virtual torque for the system, and have different effects on the existence of positive and negative sequence equilibrium points under different working conditions. T^+_{v+}, T^*_{v+}, T^-_{v-}, and T^*_{v-} must satisfy the Criterion (14) to ensure that the VSC system has the ability to achieve $T^*_{v\pm}=T^{\pm}_{v\pm}$. Otherwise, the positive and negative sequence equilibrium points of the VSC system will not exist, and the LOS phenomena will inevitably occur.

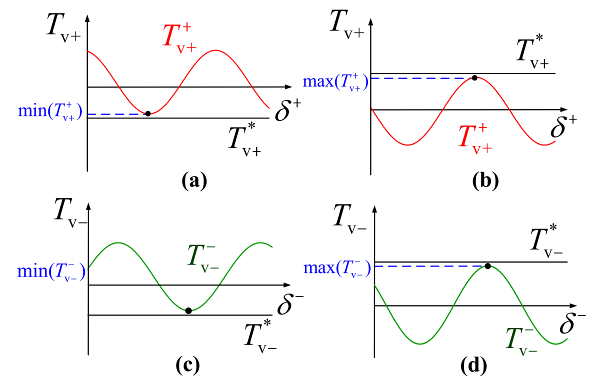

Fig. 6 **a** The min (T^+_{v+}) is greater than T^*_{v+}. **b** The max (T^+_{v+}) is less than T^*_{v+}. **c** The min (T^-_{v-}) is greater than T^*_{v-}. **d** The max (T^-_{v-}) is less than T^*_{v-}

$$\begin{aligned}&\left[\max(T^+_{v+}) \geq T^*_{v+}\right] \cap \left[\min(T^+_{v+}) \leq T^*_{v+}\right]\\&\&\&\left[\max(T^-_{v-}) \geq T^*_{v-}\right] \cap \left[\min(T^-_{v-}) \leq T^*_{v-}\right]\end{aligned} \tag{14}$$

The existence of positive and negative sequence equilibrium points of the system can be effectively evaluated by criterion (14). However, even if criterion (14) is satisfied, inappropriate transient synchronous behavior of the VSC system may lead to the deceleration or acceleration area insufficient to reach the desired equilibrium point during the transient synchronous process [9]. Therefore, it is necessary to further discuss the influence of control switching action detection delay and the interaction between the positive and negative sequence PLL on the synchronous capability of the VSC system.

3.3 Equal area criterion of the VSC system during asymmetric grid faults

Integrating both sides of (10) with δ^+ and δ^-, respectively, yields (15), where δ^+_t and δ^-_t are the respective equivalent power angles of the positive and negative sequence operating points at any instant.

In (15), ΔE_{P+} and ΔE_{P-} are the virtual potential energies due to the change of current references. ΔE^+_{K+} and ΔE^-_{K-} are the virtual kinetic energy variations of the positive and negative sequence operating points, respectively, and represent the motion state of $\omega^{\pm}_{pll}$ relative to ω_g. ΔE^-_{K+} and ΔE^+_{K-} are the virtual kinetic energy variations generated by the positive and negative sequence coupled components, respectively. ΔE^+_{D+} and ΔE^-_{D-} are the energies consumed by the positive and negative virtual damping, respectively, while $\Delta E_{\mathrm{D}+}^{-}$ and $\Delta E_{\mathrm{D}-}^{+}$ are the respective energies consumed by the positive and negative coupled virtual damping.

accumulated and released by the positive sequence operating point during the pre-fault to fault duration stage can be represented by the acceleration area ($S_{\mathrm{acc1+}}$) and deceleration area ($S_{\mathrm{dec1+}}$), respectively.

$$\begin{cases} \underbrace{\int_{\delta_0^+}^{\delta_t^+}(T_{\mathrm{v}+}^{*}-T_{\mathrm{v}+}^{+})d\delta^+}_{\Delta E_{P+}} - \underbrace{\int_{\delta_0^+}^{\delta_t^+}D_{\mathrm{v}+}^{+}(\omega_{\mathrm{pll}}^{+}-\omega_{\mathrm{g}})d\delta^+}_{\Delta E_{\mathrm{D}+}^{+}} + \underbrace{\int_{\delta_0^+}^{\delta_t^+}D_{\mathrm{v}+}^{-}(\omega_{\mathrm{pll}}^{-}+\omega_{\mathrm{g}})\Big|_{\delta_0^-}^{\delta_t^-}d\delta^+}_{\Delta E_{\mathrm{D}+}^{-}} = \underbrace{\frac{1}{2}\omega_{\mathrm{b}}J_{\mathrm{v}+}^{+}(\omega_{\mathrm{pll}}^{+}-\omega_{\mathrm{g}})^2\Big|_{\delta_0^+}^{\delta_t^+}}_{\Delta E_{\mathrm{K}+}^{+}} + \underbrace{\frac{1}{\omega_{\mathrm{b}}}\int_{\delta_0^-}^{\delta_t^-}J_{\mathrm{v}+}^{-}\delta^-\Big|_{\delta_0^-}^{\delta_t^-}d\delta^+}_{\Delta E_{\mathrm{K}+}^{-}} \\ \underbrace{\int_{\delta_0^-}^{\delta_t^-}(T_{\mathrm{v}-}^{*}-T_{\mathrm{v}-}^{-})d\delta^-}_{\Delta E_{\mathrm{P}-}} - \underbrace{\int_{\delta_0^-}^{\delta_t^-}D_{\mathrm{v}-}^{-}(\omega_{\mathrm{pll}}^{-}+\omega_{\mathrm{g}})d\delta^-}_{\Delta E_{\mathrm{D}-}^{-}} + \underbrace{\int_{\delta_0^-}^{\delta_t^-}D_{\mathrm{v}-}^{+}(\omega_{\mathrm{pll}}^{+}-\omega_{\mathrm{g}})\Big|_{\delta_0^+}^{\delta_t^+}d\delta^-}_{\Delta E_{\mathrm{D}-}^{+}} = \underbrace{\frac{1}{2}\omega_{\mathrm{b}}J_{\mathrm{v}-}^{-}(\omega_{\mathrm{pll}}^{-}+\omega_{\mathrm{g}})^2\Big|_{\delta_0^-}^{\delta_t^-}}_{\Delta E_{\mathrm{K}-}^{-}} + \underbrace{\frac{1}{\omega_{\mathrm{b}}}\int_{\delta_0^-}^{\delta_t^-}J_{\mathrm{v}-}^{+}\delta^+\Big|_{\delta_0^+}^{\delta_t^+}d\delta^-}_{\Delta E_{\mathrm{K}-}^{+}} \end{cases} \quad (15)$$

In addition, Eq. (15) indicates that because of the existence of coupled relationship between the positive and negative sequence components, the negative sequence components will affect not only the dynamic change of positive sequence equivalent power angle (δ^+), but also the conversion relationship among the virtual kinetic, potential and damping energies during the transient synchronous process of the positive sequence operating point, and vice versa. Therefore, the influence mechanism of the coupled relationship between the positive and negative sequence PLL on the synchronous capability of the VSC system needs to be further explored.

3.4 Influence on the synchronous process of the positive and negative sequence operating points

According to (10) and (13), the synchronous processes of the positive and negative sequence operating points during asymmetric grid faults are shown in Figs. 7 and 8, respectively.

In Fig. 7, $B_0 \rightarrow B_1$ is the fault detection stage, $T_{\mathrm{v0+}}^{*}$ and T_{v0} are the virtual prime mover torque and electromagnetic torque at the pre-fault stage, respectively. $T_{\mathrm{v1+}}^{*}$ is the positive sequence virtual prime mover torque at the fault detection stage, and $T_{\mathrm{v1+}}^{+}$ is the positive sequence virtual electromagnetic torque during the SLG gird fault. In Fig. 8, $B_0' \rightarrow B_1'$ is the fault detection stage, and point A_0' is the initial point of the negative sequence operating point when the SLG fault occurs, which does not exist at the pre-fault stage. $T_{\mathrm{V1}\text{-}}^{-}$ is the negative sequence virtual electromagnetic torque during the SLG gird fault. $T_{\mathrm{v1}-}^{*}$ and $T_{\mathrm{v2}-}^{*}$ are the negative sequence virtual prime mover torque during the fault detection stage and fault duration stages respectively.

According to [14], the positive sequence operating point will accelerate at the fault detection stage and then decelerate during the $B_1 \rightarrow C_1$ stage. The energy

These are shown in Fig. 7. Similarly, according to (13), the negative sequence operating point will accelerate at the fault detection stage, and decelerate at the stage of $B_1' \rightarrow C_1'$. From the pre-fault to fault duration stage, the energy accumulated and released by the negative sequence operating point can be represented by the acceleration area ($S_{\mathrm{acc1-}}$) and the deceleration area ($S_{\mathrm{dec1-}}$), as shown in Fig. 8.

It can be seen from (15) and Fig. 5 that if the unbalanced energy generated by the system during the fault detection stage cannot be completely consumed before δ^+ reaches $\delta_{\max}^{+}$, or δ^- reaches $\delta_{\max}^{-}$, the LOS phenomena

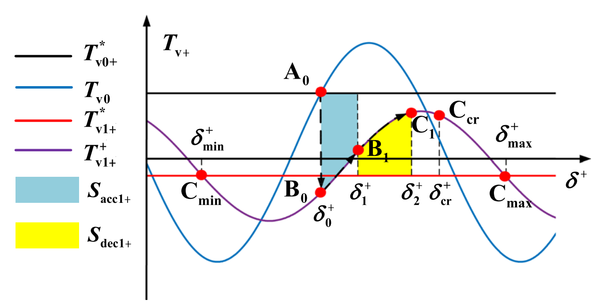

Fig. 7 Trajectories of the positive sequence operating point from pre-fault to fault duration stage

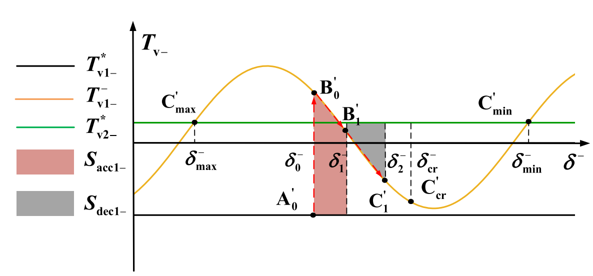

Fig. 8 Trajectories of the negative sequence operating point from pre-fault to fault duration stage

for angular frequency increase will occur in the positive and negative sequence PLL. Therefore, the transient stability criterion of the VSC system from the pre-fault to fault duration stage is expressed as:

$$\begin{cases} S_{\mathrm{acc1+}} = \int_{\delta_0^+}^{\delta_1^+} (T_{\mathrm{v0+}}^* - T_{\mathrm{v1+}}^+) d\delta^+ \\ \max(S_{\mathrm{dec1+}}) = \int_{\delta_1^+}^{\delta_{\max}^+} (T_{\mathrm{v1+}}^+ - T_{\mathrm{v1+}}^*) d\delta^+ \\ \max(\Delta E_{\mathrm{D1+}}) = \int_{\delta_0^+}^{\delta_1^+} D_{\mathrm{v1+}}^+ (\omega_{\mathrm{pll}}^+ - \omega_{\mathrm{g}}) d\delta^+ + \int_{\delta_1^+}^{\delta_{\max}^+} D_{\mathrm{v2+}}^+ (\omega_{\mathrm{pll}}^+ - \omega_{\mathrm{g}}) d\delta^+ \\ \qquad + \int_{\delta_1^+}^{\delta_{\max}^+} D_{\mathrm{v2+}}^- (\omega_{\mathrm{pll}}^- + \omega_{\mathrm{g}}) \Big|_{\delta_1^-}^{\delta_{\min}^-} d\delta^+ \\ S_{\mathrm{acc1-}} = \int_{\delta_0^-}^{\delta_1^-} (T_{\mathrm{v1-}}^- - T_{\mathrm{v1-}}^*) d\delta^- \\ \max(S_{\mathrm{dec1-}}) = \int_{\delta_1^-}^{\delta_{\min}^-} (T_{\mathrm{v2-}}^* - T_{\mathrm{v1-}}^-) d\delta^- \\ \max(\Delta E_{\mathrm{D1-}}) = \int_{\delta_0^-}^{\delta_1^-} D_{\mathrm{v1-}}^+ (\omega_{\mathrm{pll}}^+ - \omega_{\mathrm{g}}) \Big|_{\delta_0^+}^{\delta_1^+} d\delta^- + \int_{\delta_0^-}^{\delta_1^-} D_{\mathrm{v1-}}^- (\omega_{\mathrm{pll}}^- + \omega_{\mathrm{g}}) d\delta^- \\ \qquad + \int_{\delta_1^-}^{\delta_{\min}^-} D_{\mathrm{v2-}}^- (\omega_{\mathrm{pll}}^- + \omega_{\mathrm{g}}) d\delta^- + \int_{\delta_1^-}^{\delta_{\min}^-} D_{\mathrm{v2-}}^+ (\omega_{\mathrm{pll}}^+ - \omega_{\mathrm{g}}) \Big|_{\delta_1^+}^{\delta_{\max}^+} d\delta^- \\ S_{\mathrm{acc1+}} \le \max(S_{\mathrm{dec1+}} + \Delta E_{\mathrm{D1+}}) \&\& S_{\mathrm{acc1-}} \le \max(S_{\mathrm{dec1-}} + \Delta E_{\mathrm{D1-}}) \end{cases} \tag{16}$$

According to (10) and (16), from the pre-fault to fault duration stage, the existence of the positive and negative sequence coupled components will increase the positive and negative sequence deceleration areas and the energy consumed by the virtual damping. This will prevent the system from having angular frequency increase LOS phenomena.

As shown in (13), the positive sequence PLL plays a dominant role in the transient stability of the VSC system at the fault detection stage. Therefore, the critical fault clearance angle (δ_{cr}) of the system can be approximated as the critical fault clearance angle of the positive sequence operating point. Considering the influence of the negative sequence coupled components on the positive sequence critical fault clearance angle, the critical fault clearance angle (δ_{cr}) of the VSC system can be approximately derived from (17).

$$\begin{aligned} \delta_{\mathrm{cr}} = & \frac{U_{\mathrm{gf}}^+ |K_1| (\cos(\delta_0^+ - \varphi_1) - \cos(\delta_{\max}^+ - \varphi_1)) + (\omega_{\mathrm{g}} L_{\mathrm{eq4}} I_{\mathrm{dm}} + \frac{k_{\mathrm{p}}}{k_{\mathrm{i}}} L_{\mathrm{eq4}} I_{\mathrm{dm}}) \delta_0^+}{\omega_{\mathrm{g}} L_{\mathrm{eq4}} I_{\mathrm{dm}} - R_{\mathrm{eq4}} I_{\mathrm{q+}}^{+*} - \omega_{\mathrm{g}} L_{\mathrm{eq4}} I_{\mathrm{d+}}^{+*} + R_{\mathrm{eq5}} I_{\mathrm{q+}}^{-*} + \omega_{\mathrm{g}} L_{\mathrm{eq5}} I_{\mathrm{d+}}^{-*} + \frac{k_{\mathrm{p}}}{k_{\mathrm{i}}} (L_{\mathrm{eq4}} (I_{\mathrm{dm}} - I_{\mathrm{d+}}^{+*}) - L_{\mathrm{eq5}} I_{\mathrm{d+}}^{*-} (\omega_{\mathrm{pll}}^- + \omega_{\mathrm{g}}) \Big|_{\delta_1^-}^{\delta_2^-})} \\ & - \frac{-((R_{\mathrm{eq4}} I_{\mathrm{q+}}^{+*} + \omega_{\mathrm{g}} L_{\mathrm{eq4}} I_{\mathrm{d+}}^{+*} + \frac{k_{\mathrm{p}}}{k_{\mathrm{i}}} (L_{\mathrm{eq4}} I_{\mathrm{d+}}^{+*} + L_{\mathrm{eq5}} I_{\mathrm{d+}}^{-*} (\omega_{\mathrm{pll}}^- + \omega_{\mathrm{g}}) \Big|_{\delta_1^-}^{\delta_2^-}) - R_{\mathrm{eq5}} I_{\mathrm{q+}}^{-*} - \omega_{\mathrm{g}} L_{\mathrm{eq5}} I_{\mathrm{d+}}^{-*}) \delta_{\max}^+)}{\omega_{\mathrm{g}} L_{\mathrm{eq4}} I_{\mathrm{dm}} - R_{\mathrm{eq4}} I_{\mathrm{q+}}^{+*} - \omega_{\mathrm{g}} L_{\mathrm{eq4}} I_{\mathrm{d+}}^{+*} + R_{\mathrm{eq5}} I_{\mathrm{q+}}^{-*} + \omega_{\mathrm{g}} L_{\mathrm{eq5}} I_{\mathrm{d+}}^{-*} + \frac{k_{\mathrm{p}}}{k_{\mathrm{i}}} (L_{\mathrm{eq4}} (I_{\mathrm{dm}} - I_{\mathrm{d+}}^{+*}) - L_{\mathrm{eq5}} I_{\mathrm{d+}}^{*-} (\omega_{\mathrm{pll}}^- + \omega_{\mathrm{g}}) \Big|_{\delta_1^-}^{\delta_2^-})} \end{aligned} \tag{17}$$

Simplifying (17) and then combined with (16), the critical fault clearance time (t_{cut}) can be obtained, and is expressed as:

$$t_{\mathrm{cut}} = (\delta_{\mathrm{cr}} - \delta_0^+) \sqrt{\frac{2J_{\mathrm{v1+}}^+}{\omega_b (S_{\mathrm{acc1+}} - \Delta E_{\mathrm{D1+}})}} \tag{18}$$

Equation (18) means that the fault detection time must be less than t_{cut}. Otherwise, there will be LOS phenomena for angular frequency increase in the positive and negative sequence PLL.

3.5 Transient stability enhancement control strategy based on improved PLL

From the above analysis, it can be deduced that during the asymmetric faults, irrational control strategy switching delay will lead to LOS phenomena of the system. Therefore, to improve the transient stability of the VSC system during asymmetric faults by increasing the critical fault clearance time and reducing the operation delay time of the system, a transient synchronous stability enhancement control strategy of the VSC system during asymmetric grid faults is studied in this section.

It can be seen from (16)–(18) that the larger J_{v+}^+ or $\Delta E_{\mathrm{D+}}$ is, the slower the change of δ^+ and the larger the allowable the critical fault clearance time angle or time are. This makes the transient synchronous ability of the system stronger during asymmetric grid faults. To increase J_{v+}^{+} and ΔE_{D+} of the VSC system, the deviations between ω_{pll}^{+} and ω_g, and between ω_{pll}^{-} and ω_g are fed back negatively to the positive and negative sequence q-axis voltages by the amplifying parameters, respectively, as shown in Fig. 9.

According to (4) and Fig. 9, the positive and negative sequence q-axis voltage can be expressed as:

$$\begin{cases} u_{tq+}^{+} = -U_{gf}^{+}|K_1|\cos(\delta^{+}-\varphi_1) + L_{eq4}I_{d+}^{+}\omega_{pll}^{+} - L_{eq5}I_{d+}^{-}\omega_{pll}^{-} - k_{pf}(\omega_{pll}^{+}-\omega_g) \\ u_{tq-}^{-} = -U_{gf}^{-}|K_7|\cos(\delta^{-}-\varphi_7) + L_{eq9}I_{d-}^{-}\omega_{pll}^{-} - L_{eq10}I_{d-}^{+}\omega_{pll}^{+} - k_{pf}(\omega_{pll}^{-}+\omega_g) \end{cases} \tag{19}$$

By substituting (19) into (10), Eq. (20) can be obtained.

Under the control structure of Fig. 9, the critical fault clearance time of the system can be expressed as:

$$\begin{cases} \Big(\underbrace{\frac{1-k_pL_{eq4}I_{d+}^{+}}{k_i}}_{J_{v+}^{+}} + \underbrace{\frac{k_{pf}}{k_i}}_{J_{vf+}^{+}}\Big)\frac{d\omega_{pll}^{+}}{dt} + \underbrace{\frac{k_pL_{eq5}I_{d+}^{-}}{k_i}}_{J_{v+}^{-}}\frac{d\omega_{pll}^{-}}{dt} = \underbrace{R_{eq4}I_{q+}^{+} + \omega_gL_{eq4}I_{d+}^{+} - R_{eq5}I_{q+}^{-} - \omega_gL_{eq5}I_{d+}^{-}}_{T_{v+}^{*}} - \underbrace{U_{gf}^{+}|K_1|\sin(\delta^{+}-\varphi_1)}_{T_{v+}^{+}} + \underbrace{\Big(\frac{k_p}{k_i}L_{eq5}I_{d+}^{-}\Big)}_{D_{v+}^{-}}(\omega_{pll}^{-}+\omega_g) \\ -\underbrace{\Big(\frac{k_p}{k_i}(\omega_bU_{gf}^{+}|K_1|\cos(\varphi_1-\delta^{+}) - L_{eq4}I_{d+}^{+}) + k_{pf}\Big)}_{D_{v+}^{+}+D_{vf+}^{+}}(\omega_{pll}^{+}-\omega_g) \\ \Big(\underbrace{\frac{1-k_pL_{eq9}I_{d-}^{-}}{k_i}}_{J_{v-}^{-}} + \underbrace{\frac{k_{pf}}{k_i}}_{J_{vf-}^{-}}\frac{d\omega_{pll}^{-}}{dt} + \underbrace{\frac{k_pL_{eq10}I_{d-}^{+}}{k_i}}_{J_{v-}^{+}}\frac{d\boldsymbol{\omega}_{pll}^{+}}{dt} = \underbrace{(R_{eq9}I_{q-}^{-} - \omega_gL_{eq9}I_{d-}^{-} - R_{eq10}I_{q-}^{+} - \omega_gL_{eq10}I_{d-}^{+})}_{T_{v-}^{*}} - \underbrace{U_{gf}^{-}|K_7|\sin(\delta^{-}-\varphi_7)}_{T_{v-}^{-}} + \underbrace{\Big(\frac{k_p}{k_i}L_{eq10}I_{d-}^{+}\Big)}_{D_{v-}^{+}}(\omega_{pll}^{+}-\omega_g) \\ -\underbrace{\Big(\frac{k_p}{k_i}(\omega_bU_{gf}^{-}|K_7|\cos(\varphi_7-\delta^{-}) - L_{eq9}I_{d-}^{-}) + k_{pf}\Big)}_{D_{v-}^{-}+D_{vf-}^{-}}(\omega_g+\omega_{pll}^{-}) \end{cases} \tag{20}$$

$$\begin{cases} \hat{t}_{cut} = (\delta_{cr}^{+}-\delta_0^{+})\sqrt{\frac{2J_{v1+}^{+}+J_{vf+}^{+}}{\omega_b(S_{acc1+}-\Delta E_{D1+}-\Delta E_{Df+})}} \\ \Delta E_{Df+} = \int_{\delta_0^{+}}^{\delta_1^{+}} D_{vf+}^{+}(\omega_{pll}^{+}-\omega_g)d\delta^{+} + \int_{\delta_1^{+}}^{\delta_{max}^{+}} D_{vf+}^{+}(\omega_{pll}^{+}-\omega_g)d\delta^{+} \end{cases} \tag{21}$$

As shown in (21), the introduction of the negative feedback branches can effectively increase t_{cut} of the system, which means that the system can maintain transient synchronous stability with the grid under a longer fault detection delay. Therefore, this method can improve the transient synchronous stability of the VSC system during asymmetric grid faults.

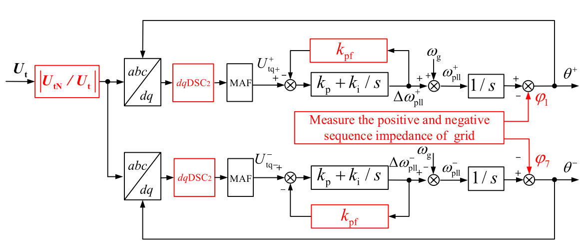

Fig. 9 The improved positive and negative sequence PLL control structure

In addition, reference [33] points out that the use of MAF in Fig. 4 will introduce signal delay to the system, which will reduce the dynamic response speed of the PLL. Therefore, an improved DSC-PLL structure is proposed based on delay signal cancellation (DSC) [34]. However, reference [34] does not consider the influence of voltage amplitude and phase angle mutation on the dynamic performance of PLL during grid fault, nor the differences of output characteristics between the positive and negative sequence PLL.

Therefore, this paper further considers the influence of K_{i} and ϕ_{i} in (3), by introducing the ratio between the rated voltage amplitude ($\boldsymbol{U}_{\mathrm{tN}}$) and the fault voltage amplitude ($\boldsymbol{U}_{\mathrm{t}}$), so the influence of the terminal voltage amplitude mutation on the transient characteristics of the positive and negative sequence PLL is weakened. Besides, to reduce the influence of the grid impedance phase angle mutation on the dynamic performance of the VSC system, the sequence impedance measurement method [35, 36] is used to introduce the positive and negative sequence impedance angles into the output angles of the positive and negative sequence PLL. Through the above methods, the dynamic response speed of the positive and negative sequence PLL for the VSC system can be further improved during asymmetric grid faults. The specific improvement measures are also shown in Fig. 9.

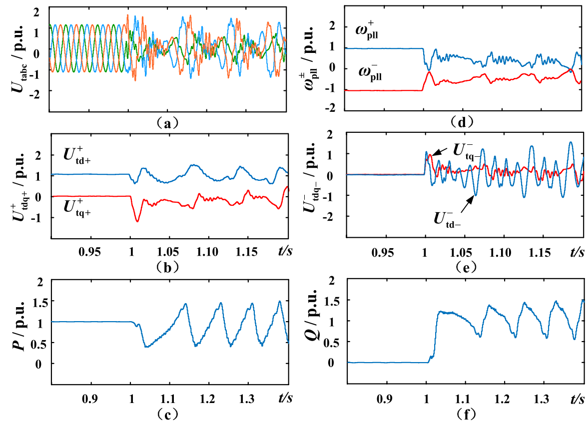

Fig. 10 Simulation results of Case 1. **a** Terminal three-phase voltage. **b** Positive sequence dq-axis voltage. **c** Output active power. **d** Positive and negative sequence PLL output frequency. **e** Negative sequence dq-axis voltage. **f** Output reactive power

4 Simulation and experimental validation

4.1 Simulation validation

In order to verify the correctness of the theoretical analysis and the effectiveness of the enhancement control strategy, a simulation model of a 2 MW PLL-based VSC grid-connected system is established in MATLAB/Simulink, which is similar to Fig. 1. The main parameters of the simulated system are listed in Table 1 in the Appendix. At the pre-fault stage, $P^{*}_{\mathrm{ref}}=1.0$ p.u., and at $t=1.0$ s, an SLG fault occurs at the 220 kV AC grid side, which causes $|\boldsymbol{U}_{\mathrm{fa}}|$ to drops to 0.32 p.u. The fault is cleared at $t=2.0$ s.

When the fault detection delay of the VSC system is 5 ms, Figs. 10–12 show the three LOS phenomena under different LVRT current references, respectively.

Case 1: When the LVRT current references $I_{\mathrm{d+}}^{+*}$, $I_{\mathrm{q+}}^{+*}$, $I_{\mathrm{d-}}^{-*}$, and $I_{\mathrm{q-}}^{-*}$ of the system are set to 0 p.u., 1 p.u., 0 p.u., and 0 p.u., respectively, according to criterion (14), the positive sequence equilibrium point of the system does not exist. Consequently, as shown in Fig. 10, the LOS phenomenon for angular frequency decrease occurs in the positive sequence PLL, and the LOS phenomenon also occurs in the negative sequence PLL owing to the influence of the positive sequence coupled components. Meanwhile, the output active and reactive power of the VSC system are also unstable due to the LOS of positive and negative sequence PLL.

Case 2: The LVRT current references $I_{\mathrm{d+}}^{+*}$, $I_{\mathrm{q+}}^{+*}$, $I_{\mathrm{d-}}^{-*}$, and $I_{\mathrm{q-}}^{-*}$ are set to − 1.0 p.u., 0.15 p.u., 0 p.u., and 0.15 p.u., respectively, and according to Criterion (16), the calculation result of $S_{\mathrm{acc1+}}$ is 0.233, while ΔS_{1+} ($\Delta S_{1+}=S_{\mathrm{dec+}}+\Delta E_{\mathrm{D1+}}$) is 0.186. As shown in Fig. 11, due to the excessive acceleration area $S_{\mathrm{acc1+}}$, the LOS phenomena for angular frequency increase occur in the positive and negative sequence PLL. Consequently, the output active and reactive power of the VSC system are

Table 1 Parameters of the simulation VSC system

Parameter	Value	Parameter	Values
Rated Power	2 MW	$Z_{\mathrm{T1}}^{+}=Z_{\mathrm{T1}}^{-}=Z_{\mathrm{T1}}^{0}$	0.005 + j0.21 p.u
Rated voltage	220 kV	$Z_{\mathrm{T2}}^{+}=Z_{\mathrm{T2}}^{-}=Z_{\mathrm{T2}}^{0}$	0.018 + j0.29 p.u
DC-link voltage	1200 V	Fault impedance Z_f	0.00027 p.u
C_f, L_f	0.0015 p.u., 0.002 p.u	$k_{\mathrm{p\_PLL}}$, $k_{\mathrm{i\_PLL}}$	0.8, 15
$Z^{+}_{\mathrm{L}}=Z^{-}_{\mathrm{L}}=Z^{0}_{\mathrm{L}}$	0.0049 + j0.32 p.u	k_p, k_i of current loop	2.5, 20

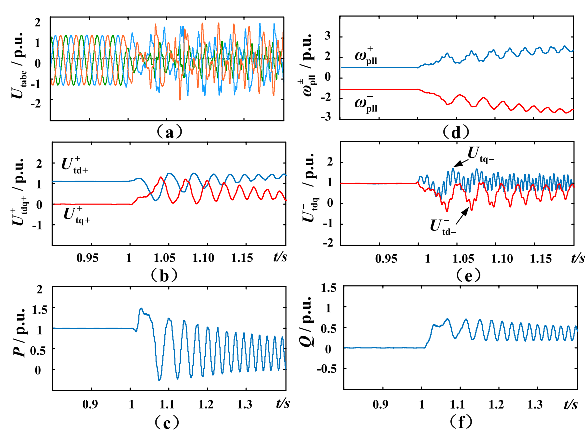

Fig. 11 Simulation results of Case 2. **a** Terminal three-phase voltage. **b** Positive sequence dq-axis voltage. **c** Output active power. **d** Positive and negative sequence PLL output frequency. **e** Negative sequence dq-axis voltage. **f** Output reactive power

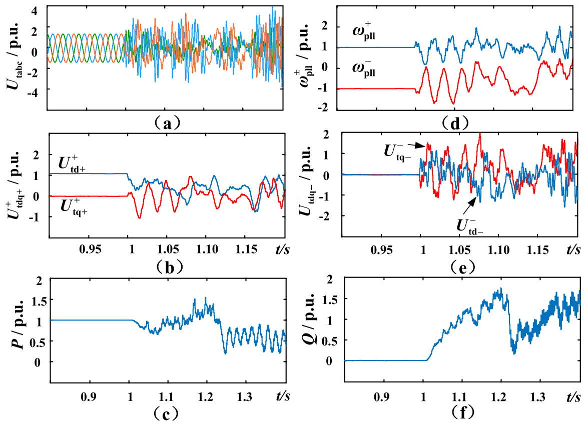

Fig. 12 Simulation results of Case 3. **a** Terminal three-phase voltage. **b** Positive sequence dq-axis voltage. **c** Output active power. **d** Positive and negative sequence PLL output frequency. **e** Negative sequence dq-axis voltage. **f** Output reactive power

also unstable due to the LOS of positive and negative sequence PLL.

Case 3: During LVRT, the I_{d+}^{+*}, I_{q+}^{+*}, I_{d-}^{-*}, and I_{q-}^{-*} are set to 0 p.u., 0.15 p.u., 0 p.u. and 0.95 p.u., respectively, according to criterion (14), the negative sequence equilibrium point of the system does not exist. Consequently, as shown in Fig. 12, the LOS phenomena for angular frequency decrease occur in the positive and negative sequence PLL. This also leads to the instability of the output active and reactive power of the VSC system. These simulation results are consistent with the analysis results.

Figure 13 shows the simulation results of the system under the same working conditions but different fault detection delays. In Fig. 13, the LVRT current references I_{d+}^{+*}, I_{q+}^{+*}, I_{d-}^{-*}, and I_{q-}^{-*} are set to − 0.75 p.u., 0.35 p.u., 0 p.u., and 0.3 p.u., respectively. In this case, according to criterion (18), t_{cut} is 13.48 ms, which is larger than the fault detection delay of 12 ms in Case 4. It means that the energy accumulated by the positive and negative sequence operating points at the fault detection stage can be consumed completely during the fault duration stage. Therefore, the system can maintain synchronous stability with the grid. However, when the fault detection time increases to 15 ms in Case 5, criterion (18) is not satisfied. As shown in Case 5, the LOS phenomena for angular frequency increase occur in the positive and negative sequence PLL. Therefore, the criterion 18 can effectively evaluate the ability of the VSC system to maintain transient synchronous stability with the grid.

To further demonstrate the effectiveness of the improved positive and negative sequence PLL control strategy, simulations with the different control strategies are performed and the results are shown in Fig. 14. As shown, the LVRT references are set to the same as those in Fig. 13, but the fault detection time is 13 ms. Under these conditions, when the traditional DDSRF-PLL control strategy is adopted [25, 26], the LOS phenomena occur in the system, which can be seen in Fig. 14. However, when the conventional dual-sequence PLL control strategy without the proposed improvement is adopted, the LOS phenomenon does not occur in the system despite a long transient regulation process. This is because the negative sequence component also has the

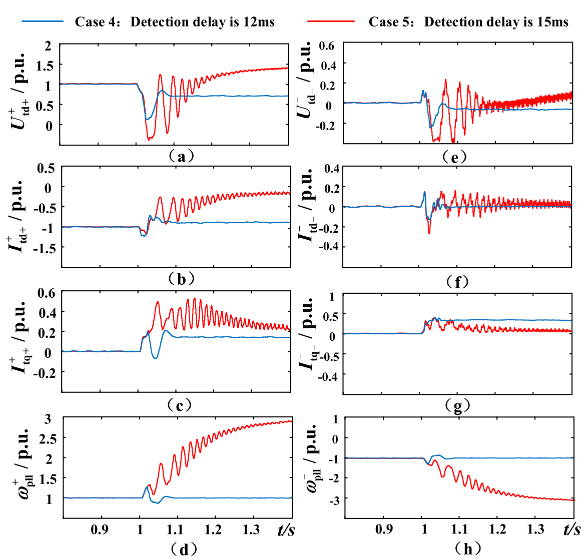

Fig. 13 Simulation results under different detection delays. **a** Positive sequence d-axis voltage. **b** Positive sequence d-axis current. **c** Positive sequence q-axis current. **d** Positive sequence PLL output frequency. **e** Negative sequence d-axis voltage. **f** Negative sequence d-axis current. **g** Negative sequence q-axis current. **h** Negative sequence PLL output frequency

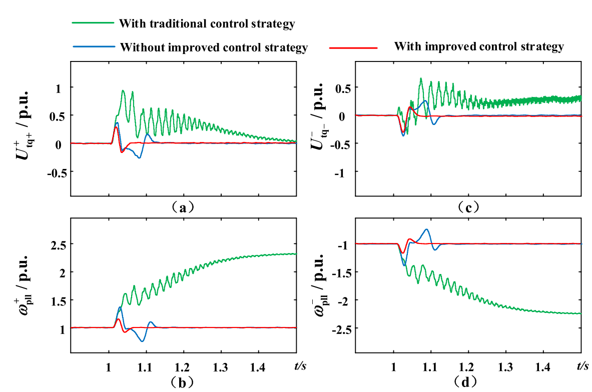

Fig. 14 Simulation results under different control strategies. **a** Positive sequence q-axis voltage. **b** Positive sequence PLL output frequency. **c** Negative sequence q-axis voltage. **d** Negative sequence PLL output frequency

ability to maintain transient synchronization with the grid, and this extends t_{cut} of the system.

In addition, as shown in Fig. 14, compared with the original control strategy. Since the improved positive and negative sequence PLL control strategy increases the virtual inertia and damping coefficient of the system, as well as compensating for the mutation of terminal voltage amplitude and phase angle during the fault, and reduces the influence of the response delay caused by MAF on the transient response characteristics of the system, it can effectively reduce the transient regulation time. It also enhances the transient synchronization performance, and increase the critical fault removal time of the system during the SLG fault. Therefore, the enhanced control strategy proposed in this paper is more beneficial for the VSC system to maintain transient synchronous stability with the grid. The simulation results are consistent with the analytical results.

Figures 15 and 16 show the simulation results of the VSC system with and without the enhancement control strategy under a two-phase-to-ground fault and two-phase fault respectively.

In Fig. 15, the two-phase-to-ground fault occurs at the 220 kV AC grid side, and the grid voltage $|\boldsymbol{U}_{ab}|$ drops to 0.6 p.u. In this case, the fault detection delay of the system is set to 9 ms, and the LVRT current references I_{d+}^{+*}, I_{q+}^{+*}, I_{d-}^{-*}, and I_{q-a}^{*} are set to − 0.4 p.u., 0.5 p.u., 0 p.u., 0.5 p.u., respectively. Under these conditions, it can be seen from (18) that the t_{cut} of the system is 8.44 ms without the improved control strategy. Consequently, the LOS phenomena occurs in the system. However, when the enhancement control strategy is adopted, according to (21), t_{cut} is extended to 9.62 ms, and the system does not have the LOS phenomenon.

Similarly, in Fig. 16, the two-phase fault occurs at the 220 kV AC grid side, and the grid voltage $|\boldsymbol{U}_{ab}|$ drops to 0.63 p.u. In this case, during LVRT, if the fault detection delay of the system is set to 11 ms and the current references I_{d+}^{+*}, I_{q+}^{+*}, I_{d-}^{-*}, and I_{q-}^{-*} are set to − 0.5 p.u., 0.4 p.u., 0 p.u., 0.45 p.u., respectively, t_{cut} is 10.62 ms without the enhancement control strategy, and thus the LOS phenomena occur. However, t_{cut} is extended to 11.35 ms with the enhancement control strategy, and the system can maintain transient synchronization with the grid. Therefore, the improved positive and negative sequence PLL control strategy can effectively increase t_{cut} and enhance the transient stability margin of the VSC system under different types of asymmetric grid faults.

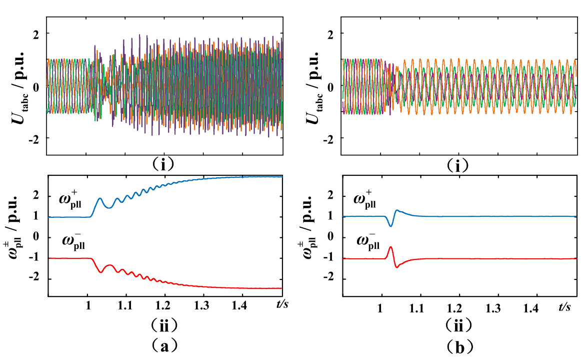

Fig. 15 Simulation results under two-phase-to-ground fault. **a** Without improved control strategy. **b** With improved control strategy. **i** Terminal three-phase voltage. **ii** Positive and negative sequence PLL output frequency

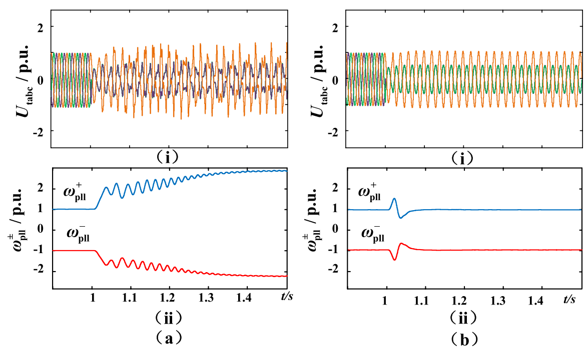

Fig. 16 Simulation results under two-phase fault. **a** Without enhancement control strategy. **b** With enhancement control strategy. **i** Terminal three-phase voltage. **ii** Positive and negative sequence PLL output frequency

4.2 Experimental validation

To verify the accuracy of the theoretical analysis and the effectiveness of the enhancement control strategy, a 2.0 kW grid-connected VSC system is configured. The detailed experimental setup is shown in Fig. 17. As illustrated in Sect. 2, the generating source can be reasonably assumed as an ideal DC voltage source, so the DC-link voltage can be maintained stable during the grid faults. Therefore, an ideal DC voltage source is used in the experiments [37]. Besides, the reactors are used to simulate the transmission line and an oscilloscope is used to

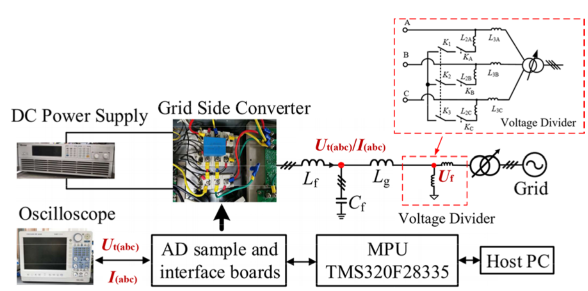

Fig. 17 Configuration of the grid-connected VSC system

Table 2 Parameters of the experimental VSC system

Parameter	Value	Parameter	Values
Rated Power	2 kW (1 p.u.)	$Z_L^+ = Z_L^- = Z^0_L$	0.14 + j0.52 p.u
Rated voltage	220 V (1 p.u.)	$Z_T^+ = Z_T^- = Z_T^0$	0.0036 + j0.026p.u
DC-link voltage	400 V	k_p, k_i of current loop	0.8, 0.1
Rated frequency	50 Hz (1 p.u.)	k_{p_PLL}, k_{i_PLL},	0.018, 0.002
$L^+_f = L^-_f$	5 mH	$k^+_{p\_PLL\_fault}$, $k^+_{i\_PLL\_fault}$	0.02, 0.005
$C^+_f = C^-_f$	30 μF	$k^-_{p\_PLL\_fault}$, $k^-_{i\_PLL\_fault}$	0.025, 0.005

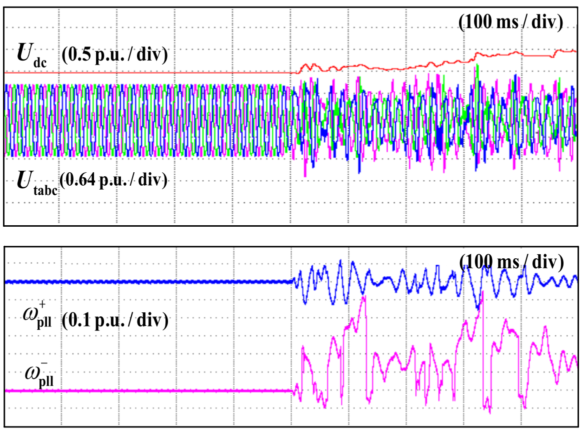

Fig. 18 Experimental results of Case 1, the LOS phenomenon of the system caused by the absence of negative sequence equilibrium point

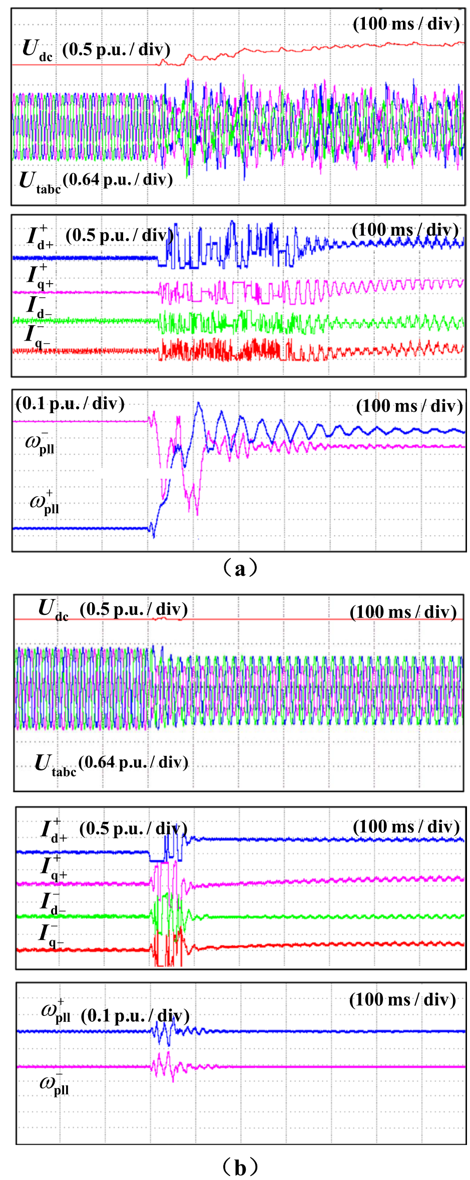

Fig. 19 Experimental results under different control strategies. **a** Case 3: without the improved control strategy. **b** Case 4: with the improved control strategy

measure the data, and the asymmetrical grid fault is realized by the voltage divider. The main parameters of the experimental system are listed in Table 2 in the Appendix. Owing to the limitation of the laboratory conditions, only the experiments for the two-phase fault are presented here. Using the voltage divider, a two-phase short-circuit fault occurs in the AC grid at $t = 1.1$ s, causing the grid voltage $|\boldsymbol{U}_{ab}|$ to drop to 0.2 p.u., and the fault is cleared at $t = 2.1$ s.

Figure 18 presents the experimental results of the LOS phenomena of the system caused by the absence of negative sequence equilibrium point during the two-phase fault. In Case 1, the LVRT current references I_{d+}^{+*}, I_{q+}^{+*}, I_{d-}^{-*}, and I_{q-}^{-*} are set to − 0.15 p.u., 0.2 p.u., 0 p.u. and 0.9 p.u., respectively. According to (10), the maximum value of T_{v-}^{-} is lower than T_{v-}^{*}, which causes criterion (14) no to be satisfied and the LOS phenomenon for angular frequency decrease in the negative sequence PLL. Due to the coupled characteristics between the positive and negative components, the LOS phenomenon also occurs in the positive sequence PLL. The experimental results are in agreement with the analytical and simulation results.

Figure 19 presents two cases of experimental results for the VSC system without and with the enhancement control strategy. The fault detection time of the system is set to 12 ms, and the LVRT current instructions $I_{\mathrm{d+}}^{+*}$, $I_{\mathrm{q+}}^{+*}$, $I_{\mathrm{d-}}^{-*}$, and $I_{\mathrm{q-}}^{-*}$ are set to − 0.65 p.u., 0 p.u., 0.3 p.u., 0.3 p.u., respectively. In these conditions, the critical fault clearance time of the system calculated by criterion (18) is 11.24 ms. It can be seen from Case 3 that the LOS phenomena occur. However, when the enhancement control strategy is adopted in Case 4, according to (21), t_{cut} is extended to 12.52 ms, which is greater than the fault detection time. Therefore, the LOS phenomenon does not occur.

All the experimental results are in agreement with the analytical and simulation results. In addition, since the differences among different types of asymmetric grid faults are mainly reflected in the structure of the sequence domain circuit, this does not affect the modeling of the two-phase fault or two-phase-to-ground fault. Therefore, the model and conclusions drawn in this paper are applicable to different types of asymmetric grid faults.

5 Conclusion

In this paper, the transient synchronous stability of the PLL-based grid-connected VSC system during asymmetric grid faults is studied. Through theoretical analysis, simulation and experimental verification, the following conclusions are drawn:

1. The interaction mechanism between the positive and negative sequence PLL during asymmetric grid faults is analyzed. The results show that under the action of the impedance network, the coupled relationship will be generated between the positive and negative sequence components. Consequently, the dynamic behaviors of the positive and negative sequence PLL will affect each other. Therefore, the VSC system can maintain transient stability with the grid only when there are no LOS phenomena both in the positive and negative sequence PLL.
2. The influence of sequence control switching action, detection delay and interaction between the positive and negative sequence PLL on the transient synchronous stability of the VSC system are analyzed, and the criteria of transient synchronous stability based on the critical fault removal angle and time are derived. The analysis results show that the imbalance of the virtual energy accumulated or released by the positive and negative sequence operating points, and long detection delay can lead to LOS phenomena. Besides, the instability criteria proposed in this paper can effectively evaluate the transient synchronous stability of the VSC system during asymmetric grid faults.
3. A transient synchronous stability enhancement control strategy based on improved positive and negative sequence PLL for the VSC system during asymmetric grid faults is proposed. Simulation and experimental results show that the proposed method can effectively increase the critical fault removal time of the system, and enhance the transient synchronous stability of the VSC system under different types of asymmetric grid faults.

Appendix

Detailed expressions of coefficient in (3).

$$
\begin{aligned}
&K_1=\frac{Z_{\mathrm{t}}^{+}}{Z_{\mathrm{l}}^{+}+Z_{\mathrm{t}}^{+}},K_2=\frac{Z_{\mathrm{t}}^{+}}{Z_{\mathrm{l}}^{+}+Z_{\mathrm{t}}^{+}+3Z_{\mathrm{f}}+Z_{\mathrm{l}}^{0}},K_3=\frac{Z_{\mathrm{t}}^{+}}{Z_{\mathrm{l}}^{+}+Z_{\mathrm{t}}^{+}+3Z_{\mathrm{f}}+Z_{\mathrm{t}}^{-}+Z_{\mathrm{l}}^{-}},\\
&K_6=\frac{Z_{\mathrm{t}}^{-}}{Z_{\mathrm{l}}^{-}+Z_{\mathrm{t}}^{-}+3Z_{\mathrm{f}}+Z_{\mathrm{l}}^{0}},K_7=\frac{Z_{\mathrm{t}}^{-}}{Z_{\mathrm{l}}^{-}+Z_{\mathrm{t}}^{-}},K_8=\frac{Z_{\mathrm{t}}^{-}}{Z_{\mathrm{l}}^{+}+Z_{\mathrm{t}}^{+}+3Z_{\mathrm{f}}+Z_{\mathrm{t}}^{-}+Z_{\mathrm{l}}^{-}},\\
&Z_4=Z_{\mathrm{t}}^{+}//(Z_{\mathrm{l}}^{+}+Z_{\mathrm{t}}^{0}+Z_{\mathrm{t}}^{-}+3Z_{\mathrm{f}}+Z_{\mathrm{l}}^{-}),\\
&Z_5=(Z_{\mathrm{t}}^{-}//(Z_{\mathrm{l}}^{+}+Z_{\mathrm{t}}^{0}+Z_{\mathrm{t}}^{+}+3Z_{\mathrm{f}}+Z_{l}^{-}))\frac{Z_{\mathrm{t}}^{+}}{Z_{\mathrm{l}}^{+}+Z_{\mathrm{t}}^{+}+Z_{\mathrm{t}}^{0}+3Z_{\mathrm{f}}+Z_{\mathrm{t}}^{-}},
\end{aligned}
$$

$$
\begin{aligned}
&Z_9=Z_{\mathrm{t}}^{-}//(Z_{\mathrm{l}}^{-}+Z_{\mathrm{t}}^{0}+Z_{\mathrm{t}}^{+}+3Z_{\mathrm{f}}+Z_{\mathrm{l}}^{+}),\\
&Z_{10}=(Z_{\mathrm{t}}^{+}//(Z_{\mathrm{l}}^{+}+Z_{\mathrm{t}}^{0}+Z_{\mathrm{t}}^{-}+3Z_{\mathrm{f}}+Z_{\mathrm{l}}^{-}))\frac{Z_{\mathrm{t}}^{-}}{Z_{\mathrm{l}}^{+}+Z_{\mathrm{t}}^{+}+Z_{\mathrm{t}}^{0}+3Z_{\mathrm{f}}+Z_{\mathrm{l}}^{-}}.
\end{aligned}
$$

Acknowledgements
Not applicable.

Author contributions
All authors contributed to the research. YL modeled the system, designed the algorithm of control strategy, and wrote the paper. JY, SH, and SC put forward the initial concept and gave technical guidance in the whole process. ZC, and QZ check the data and experimental results, and demonstrate the strategy proposed in the article. ZQ contributed to the revision and typesetting of the manuscript. All authors read and approved the final manuscript.

Funding
This work was supported in part by the National Natural Science Foundation of China under Grant 51977019, and in part by the Joint Research Fund in Smart Grid (U1966208) under cooperative agreement between the National Natural Science Foundation of China and State Grid Corporation of China.

Availability of data and materials
All data that support the finding of this study are included in this manuscript and its supplement information files.

Declarations

Competing interests
The authors declare that they have no known competing financial interests or personal relationships that could have appeared to influence the work reported in this article.

Received: 26 December 2022 Accepted: 12 June 2023
Published online: 25 July 2023

References

1. Chang, Y., Hu, J., & Yuan, X. (2020). Mechanism analysis of DFIG-based wind turbine's fault current during LVRT with equivalent inductances. *IEEE Journal of Emerging and Selected Topics in Power Electronics, 8*(2), 1515–1527.
2. Göksu, Ö., Teodorescu, R., Bak, C. L., Iov, F., & Kjær, P. C. (2013). Impact of wind power plant reactive current injection during asymmetrical grid faults. *IET Renewable Power Generation, 7*(5), 484–492.
3. Ouyang, J., Yu, J., Long, X., et al. (2023). Coordination control method to block cascading failure of a renewable generation power system under line dynamic security. *Protection and Control of Modern Power Systems, 8*(12), 194–204.
4. Singh, S., Saini, S., & Gupta, S. K. (2023). Solar-PV inverter for the overall stability of power systems with intelligent MPPT control of DC-link capacitor voltage. *Protection and Control of Modern Power Systems, 8*(15), 245–264.
5. Gao, C., Huang, C., Zheng, W., et al. (2023). Virtual impedance brake renewable energy unit low voltage through control. *Power system protection and control, 51*(10), 142–152.
6. GB/T 19963.1-2021. Technical specification for connecting wind farm to power system—Part 1: On shore wind power.
7. VDE (Association for electrical, electronic and information technologies). (2015). VDE-AR-N 4120, Technical requirements for the connection and operation of customer installations to the high voltage network for Germany. National Legislation, Berlin, Germany.
8. National Grid ESO. (2019). Interimreport into the low frequency demand disconnection (LFDD) following generator trips and frequency excursion on 9 Aug 2019.
9. Hu, Q., Fu, L., Ma, F., & Ji, F. (2019). Large signal synchronizing instability of PLL-based VSC connected to weak AC grid. *IEEE Transactions on Power Systems, 34*(4), 3220–3229.
10. Dong, D., Wen, B., Boroyevich, D., Mattavelli, P., & Xue, Y. (2015). Analysis of phase-locked loop low-frequency stability in three-phase grid-connected power converters considering impedance interactions. *IEEE Transactions on Industrial Electronics, 62*(1), 310–321.
11. Tang, W., Hu, J., Chang, Y., & Liu, F. (2018). Modeling of DFIG-based wind turbine for power system transient response analysis in rotor speed control timescale. *IEEE Transactions on Power Systems, 33*(6), 6795–6805.
12. Pei, J., et al. (2020). Characteristic analysis and risk assessment for voltage–frequency coupled transient instability of large-scale grid-connected renewable energy plants during LVRT. *IEEE Transactions on Industrial Electronics, 67*(7), 5515–5530.
13. Huang, L., Xin, H., Wang, Z., Zhang, L., Wu, K., & Hu, J. (2019). Transient stability analysis and control design of droop-controlled voltage source converters considering current limitation. *IEEE Transactions on Smart Grid, 10*(1), 578–591.
14. Pei, J., Yao, J., Liu, Y., Chen, S., Sun, P., & Huang, S. (2022). Modeling and transient synchronization stability analysis for PLL-based renewable energy generator considering sequential switching schemes. *IEEE Transactions on Power Electronics, 37*(2), 2165–2179.
15. Ma, S., Geng, H., Liu, L., Yang, G., & Pal, B. C. (2018). Grid-synchronization stability improvement of large scale wind farm during severe grid fault. *IEEE Transactions on Power Systems, 33*(1), 216–226.
16. Joint NERC & WECC Staff Report. (2018). 900 MW fault induced solar photovoltaic resource interruption disturbance report. NERC, Atlanta, GA, USA.
17. Göksu, Ö., Teodorescu, R., Bak, C. L., Iov, F., & Kjær, P. C. (2014). Instability of wind turbine converters during current injection to low voltage grid faults and PLL frequency based stability solution. *IEEE Transactions on Power Systems, 29*(4), 1683–1691.
18. Zhang, M., & Sun, L. (2020). PLL and additional frequency control constituting an adaptive synchronization mechanism for VSCs. *IEEE Transactions on Power Systems, 35*(6), 4920–4923.
19. Kabalan, M., Singh, P., & Niebur, D. (2019). A design and optimization tool for inverter-based microgrids using large-signal nonlinear analysis. *IEEE Transactions on Smart Grid, 10*(4), 4566–4576.
20. He, X., & Geng, H. (2021). Transient stability of power systems integrated with inverter-based generation. *IEEE Transactions on Power Systems, 36*(1), 553–556.
21. Anderson, P. M. (1995). *Analysis of faulted power systems* (1st ed.). IEEE Press.
22. Liu, R., Yao, J., Sun, P., Pei, J., Zhang, H., & Zhao, Y. (2021). Complex impedance-based frequency coupling characteristics analysis of DFIG-Based WT during asymmetric grid faults. *IEEE Transactions on Industrial Electronics, 68*(9), 8274–8288.
23. He, X., He, C., Pan, S., Geng, H., & Liu, F. (2022). Synchronization instability of inverter-based generation during asymmetrical grid faults. *IEEE Transactions on Power Systems, 37*(2), 1018–1031.
24. Neumann, T., Wijnhoven, T., Deconinck, G., & Erlich, I. (2015). Enhanced dynamic voltage control of type 4 wind turbines during unbalanced grid faults. *IEEE Transactions on Energy Conversion, 30*(4), 1650–1659.
25. Guo, X., Zhang, X., Wang, B., Wu, W., & Guerrero, J. M. (2014). Asymmetrical grid fault ride-through strategy of three-phase grid-connected inverter considering network impedance impact in low-voltage grid. *IEEE Transactions on Power Electronics, 29*(3), 1064–1068.
26. Mortazavian, S., & Mohamed, Y. A. I. (2019). Analysis and augmented model-based control design of distributed generation converters with a flexible grid-support controller. *IEEE Transactions on Power Electronics, 34*(7), 6369–6387.
27. Chang, Y., Hu, J., Tang, W., & Song, G. (2018). Fault current analysis of type-3 WTs considering sequential switching of internal control and protection circuits in multi time scales during LVRT. *IEEE Transactions on Power Systems, 33*(6), 6894–6903.
28. Guo, X., Zhu, D., Hu, J., Zou, X., Kang, Y., & Guerrero, J. M. (2022). Inertial PLL of grid-connected converter for fast frequency support. *CSEE Journal of Power and Energy Systems*. https://doi.org/10.17775/CSEEJPES.2021.08650
29. Yuan, H., Xin, H., Huang, L., Wang, Z., & Wu, D. (2019). Stability analysis and enhancement of type-4 wind turbines connected to very weak grids under severe voltage sags. *IEEE Transactions on Energy Conversion, 34*(2), 838–848.
30. Tang, C. Y., Chen, Y. F., Chen, Y. M., & Chang, Y. R. (2015). DC-link voltage control strategy for three-phase back-to-back active power conditioners. *IEEE Transactions on Industrial Electronics, 62*(10), 6306–6316.

31. Golestan, S., Guerrero, J. M., & Abusorrah, A. M. (2015). MAF-PLL with phase-lead compensator. *IEEE Transactions on Industrial Electronics, 62*(6), 3691–3695.
32. Ma, C., Gao, F., He, G., & Li, G. (2015). A voltage detection method for the voltage ride-through operation of renewable energy generation systems under grid voltage distortion conditions. *IEEE Transactions on Sustainable Energy, 6*(3), 1131–1139.
33. Golestan, S., Ramezani, M., Guerrero, J. M., & Monfared, M. (2015). dq-Frame cascaded delayed signal cancellation-based PLL: Analysis, design, and comparison with moving average filter-based PLL. *IEEE Transactions on Power Electronics, 30*(3), 1618–1632.
34. Golestan, S., Freijedo, F. D., Vidal, A., Yepes, A. G., Guerrero, J. M., & Doval-Gandoy, J. (2016). An efficient implementation of generalized delayed signal cancellation PLL. *IEEE Transactions on Power Electronics, 31*(2), 1085–1094.
35. Shah, S., Koralewicz, P., Gevorgian, V., & Wallen, R. (2022). Sequence impedance measurement of utility-scale wind turbines and inverters-reference frame, frequency coupling, and MIMO /SISO forms. *IEEE Transactions on Energy Conversion, 37*(1), 75–86.
36. Cao, P., Huang, M., Wang, Y., et al. (2023). Electromagnetic transient analysis and indirect traveling wave fault location method for AC line lightning arrester ice melting fault. *Power System Protection and Control, 51*(10), 11–21.
37. Shin, D., Lee, K. J., Lee, J. P., Yoo, D. W., & Kim, H. J. (2015). Implementation of fault ride-through techniques of grid-connected inverter for distributed energy resources with adaptive low-pass notch PLL. *IEEE Transactions on Power Electronics, 30*(5), 2859–2871.